





## Gas flow regimes and transition criteria in porous media

Mingbao Zhang , Zhiguo Tian , Yunfan Huang , and Moran Wang <sup>\*</sup>  
*Department of Engineering Mechanics, Tsinghua University, Beijing 100084, China*



(Received 9 October 2024; accepted 21 January 2025; published 24 February 2025)

Traditional categorization of gas flow regimes in porous media relies phenomenally on Darcy's law, yielding phenomenologically a "pre-Darcy" flow regime and a "post-Darcy" flow regime before and after the linear region, respectively. This study redefines the classification of gas flow regimes by integrating the underlying flow mechanisms, proposing four distinct regimes: the slip regime, the Darcy regime, the inertia regime, and the turbulence regime. Through a scaling analysis of the Forchheimer equation, a dimensionless number,  $R_d$ , is introduced as a criterion for the onset of the inertia regime. The classification is validated using an independently established gas seepage experimental platform, which confirms the presence of gas slip effects in the "pre-Darcy" regime. Experimental data from the inertia regime show a linear increase of critical  $R_d$  with a rising permeability ( $R_{d,critical} \propto k$ ). The deduced critical Reynolds number,  $Re$ , further substantiates that at low permeability, gas slip effects delay the transition to the inertia regime, while at high permeability, increased pore size or decreased tortuosity may hinder the generation of inertial backflow. Furthermore, the Forchheimer equation provides a more accurate description of both the Darcy and inertia regimes compared to the cubic law, with its inertial coefficient determined through appropriate fitting correlations. This study offers valuable insights into gas flow regimes within porous media, and it provides experimental results for further reference.

DOI: [10.1103/PhysRevFluids.10.024303](https://doi.org/10.1103/PhysRevFluids.10.024303)

### I. INTRODUCTION

Gas flow in porous media occurs across various engineering fields, including unconventional gas extraction [1,2], carbon dioxide sequestration [3], nuclear waste disposal [4], and industrial applications involving porous ceramics and porous metals [5]. Accurate modeling of gas flow in porous media is important for enhancing production efficiency and application performance [6–8].

The classification of flow regimes in porous media depends on the observed relationship between pressure gradient and velocity. The earliest description of the flow regime is Darcy's law, proposed by French engineer Henry Darcy in 1856 through the experiment of water flowing through sand [9]. Darcy's law describes a linear relationship in the Darcy regime and also can be derived in various ways theoretically. However, both laboratory experiments and field applications have consistently revealed nonlinear phenomena that deviate from Darcy's law [10,11]. These deviations are attributed to effects such as inertia effects at high flow velocities [12,13] and slip effects in low-pressure micro/nanopores [14–16]. Consequently, flow regimes are commonly classified into the Darcy regime and two nonlinear regimes: the pre-Darcy regime and the post-Darcy regime [17]. The graph calibration method has been used to distinguish flow regimes with different criteria [18,19]. Subsequent constitutive equations are also modified based on Darcy's law, such as the Forchheimer equation with a quadratic non-Darcy term [20] and the cubic law with a cubic correction term [21].

---

<sup>\*</sup>Contact author: [mrwang@tsinghua.edu.cn](mailto:mrwang@tsinghua.edu.cn)

Nonetheless, it is worth noting that these definitions of flow regimes, largely based on empirical observations, lack a robust physical basis. This limitation restricts deeper insights into the complex mechanisms driving these behaviors.

The so-called pre-Darcy flow regime was initially observed in the previous low-velocity liquid seepage experiments, displaying diverse pressure gradient-velocity curves [22–26]. Several mechanisms have been proposed to explain these behaviors, including the threshold pressure gradient [24], solid-liquid interactions [27], and (electro-)osmotic effects. However, no unified constitutive equation or universally accepted criteria have been established for the pre-Darcy flow regime. In contrast, the mechanics of gas flow are relatively simpler and may provide new perspectives for understanding and classifying pre-Darcy flow behaviors.

The mechanism of post-Darcy flow is generally well understood and commonly attributed to inertial effects, but the onset criteria, which signify when significant inertial effects occur, remain controversial [28]. The apparent velocity was initially used as a criterion, combined with the hydraulic gradient or the more significant reduced pressure drop (i.e., the ratio of the pressure gradient to velocity) [18,19]. However, because the apparent velocity is affected by the properties of different fluids, researchers have favored dimensionless numbers for their simplicity and general applicability. Similar to the criteria in pipe flow, the Reynolds number  $Re$  was used to classify flow regimes naturally [11,29]. Since the pore diameter is difficult to determine as a characteristic size, the  $Re_k$  number taking the square root of permeability as the characteristic length became a good choice [19,30,31]. In addition, the Forchheimer number  $Fo$ , the ratio of the second term to the first term in the Forchheimer equation, was proposed when using the average theory to derive the Forchheimer equation [22,32–34]. However, the application of dimensionless numbers remains empirical and lacks a theoretical foundation. Furthermore, previous research results have shown a significant variation in the onset criteria for different porous samples. Detailed data are shown in Table II of Appendix.

Previous studies have largely classified fluid flow regimes based on phenomenological observations, often lacking physical significance. The onset criteria of the inertia regime are still debated and lack a theoretical foundation. Compared to liquid flow, gas seepage exhibits a clearer mechanism, yet research concerning the flow regime classification using gas remains relatively limited. The present work aims to explore the physical mechanism of gas flow regime division and theoretical support of the critical criterion. By conducting experiments on artificial cores, the study will validate the classification scheme. In light of the aforementioned issues and objectives, this work is organized into the following sections: In Sec. II, the classification of gas flow regimes is redefined by incorporating the physical mechanism of gas flow within the context of the classical pore-throat structure. Scaling analysis of the Forchheimer equation redefines a dimensionless number and explains its physical meaning and advantages. In Sec. III, the gas seepage platform developed for this study is introduced. Flow regimes are classified based on experimental data, confirming the presence of the slip regime and demonstrating the relevance of the Knudsen number. The onset criteria for the inertia regime are analyzed, proposing new criteria and providing physical explanations. Furthermore, a comparison between the Forchheimer equation and the cubic law is conducted, and empirical correlations for the inertial coefficient are provided. Finally, conclusions are presented in Sec. IV.

## II. MECHANISM ANALYSIS

### A. Flow regimes

Flow regimes have been categorized primarily around the Darcy regime based on experimental data, often neglecting the underlying mechanisms governing each specific flow regime. For unconventional flows due to special effects, e.g., nonideal gas effects or high Knudsen number effects [35,36], the flow regime can be divided based on the influence of different effects. In light of this,

we have initially synthesized the mechanisms behind each flow regime and then reevaluated the categorization of gas flow regimes.

For the pre-Darcy flow regime, the mechanisms by which gas and liquid affect the flow regime are distinctly different. The occurrence of the pre-Darcy flow regime in liquid flow can be attributed to two categories: the first is the interface scale effect, referring to the special physical and chemical phenomena that occur at the solid-liquid interface and when scale changes, including non-Newtonian phenomena resulting from changes in fluid viscosity near the solid surface [37,38] and interactions between surface charges on solid particles and liquid molecules at the interface [39,40]; the second is the structural effect, referring to the influence of changes in the internal structure of the porous medium, including entrained flow of small particles and compressive deformation of the porous structure [41]. The influence of liquid on the pre-Darcy flow regime generally increases the flow resistance and reduces the measured permeability. The reason for not including the threshold pressure gradient in this context is that, after careful examination and discussion by many researchers, it has been considered a misinterpretation of experimental data [42]. The mechanism of the pre-Darcy flow regime for gas flow is relatively easy to characterize and mainly caused by the slip effect resulting from thermodynamic nonequilibrium [43]. Therefore, the physical image and experiment use gas flow to analyze the mechanism and as validation in the following sections.

Distinct flow regimes within porous media can be visualized through the classic pore-throat structure. The mechanism of the slip regime is shown in Fig. 1(a), where the local velocity profile typically follows a parabolic shape. However, due to the small pore size and low pore pressure, the collisions between solid wall molecules and fluid molecules are insufficient to establish thermodynamic equilibrium [44]. Consequently, a slip velocity emerges adjacent to the solid wall boundary, leading to increased local flow velocity and higher apparent permeability compared to nonslip flow [45,46]. With the increase in driving pore pressure, the slip effect gradually diminishes. The flow regime shifts to the Darcy regime, as shown in Fig. 1(b). In the Darcy regime, the fluid flow becomes continuous and smooth, and the velocity profile assumes a standard parabolic configuration, representing wall-bounded creeping flow with no slip at the solid wall. Its macroscopic manifestation is a linear relationship between pressure gradient and apparent velocity. The standard linear flow regime requires several key conditions, including incompressible fluid behavior, Newtonian fluid properties, and single-phase flow. As the fluid velocity continues to increase, the inertial effect becomes significant in the inertia regime, resulting in localized inertial backflow within the pore throat [47,48], as depicted in Fig. 1(c). The fluid flow begins to show early signs of vortices and disturbance while still maintaining overall coherence. Some researchers suggest the formation of a boundary layer near the solid wall [49,50]. The development of both the boundary layer and the inertial core is thought to increase flow resistance. The local velocity profile remains a parabolic shape but becomes more rounded. The lower local mean velocity, relative to the linear increase with the pressure gradient, results in reduced apparent permeability. The three flow regimes overall exhibit laminar flow, and further development of the flow regime will result in a transition to the turbulence regime, as shown in Fig. 1(d). Several mechanisms contribute to this transition within the pore throat, including surface roughness, the mixing of intersecting streams, and the detachment of the microscopic flow field from the local geometry [51,52]. Turbulent flow is characterized by its high degree of chaos and unsteadiness [53], with curved and intersecting streamlines, as well as a flatter velocity profile compared to laminar flow. The presence of numerous recirculation zones and the resulting chaotic motion leads to a slower increase in local mean velocities compared to the inertia regime, thus reducing permeability [47]. Through the above mechanistic analysis, we delineate four distinct gas flow regimes: the slip regime, the Darcy regime, the inertia regime, and the turbulence regime. Figure 2 illustrates the apparent velocity versus pressure gradient curves for these four flow regimes.

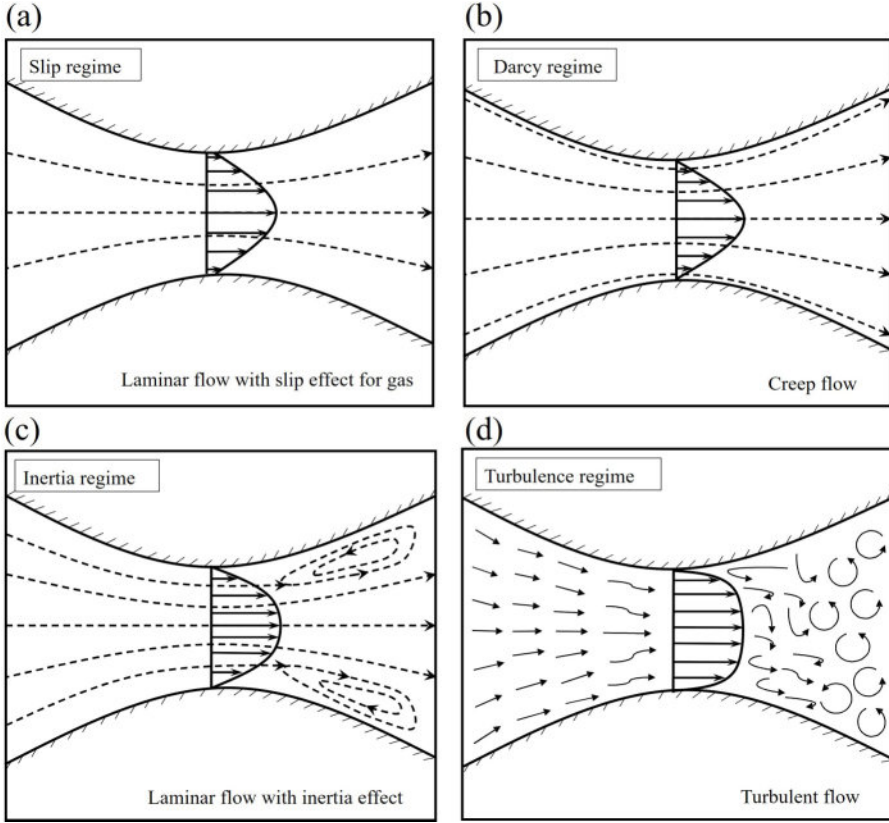


FIG. 1. Schematic of the mechanism of the four flow regimes in a classic pore-throat structure: (a) slip regime; (b) Darcy regime; (c) inertia regime; (d) turbulence regime. The velocity profiles merely serve as an illustrative representation of the flow state under steady inflow conditions, which do not present the actual flow within the pore space.

### B. Dimensionless criteria

Each flow regime requires its own unique constitutive equation for mathematical representation. The simplest of these equations, known as Darcy's law, is specifically used to describe the Darcy regime, as expressed below:

$$-\frac{\Delta P}{L} = \frac{\mu}{k}v, \quad (1)$$

where  $\Delta P$  (Pa) is the pressure difference between upstream and downstream,  $L$  (m) is the length of the sample,  $\mu$  (Pa s) is the dynamic viscosity of the fluid,  $v$  ( $\text{m s}^{-1}$ ) is the apparent velocity, and  $k$  ( $\text{m}^2$ ) is the permeability. To facilitate the display of experimental data, the permeability unit is mD. 1 mD is approximately equal to  $10^{-15} \text{ m}^2$ . The incorporation of quadratic or cubic terms into Darcy's law allows for a description of the inertial regime using the Forchheimer equation and the cubic law. The generalized Forchheimer equation is

$$-\frac{\Delta P}{L} = \frac{\mu}{k}v + \rho\beta_1v^2, \quad (2)$$

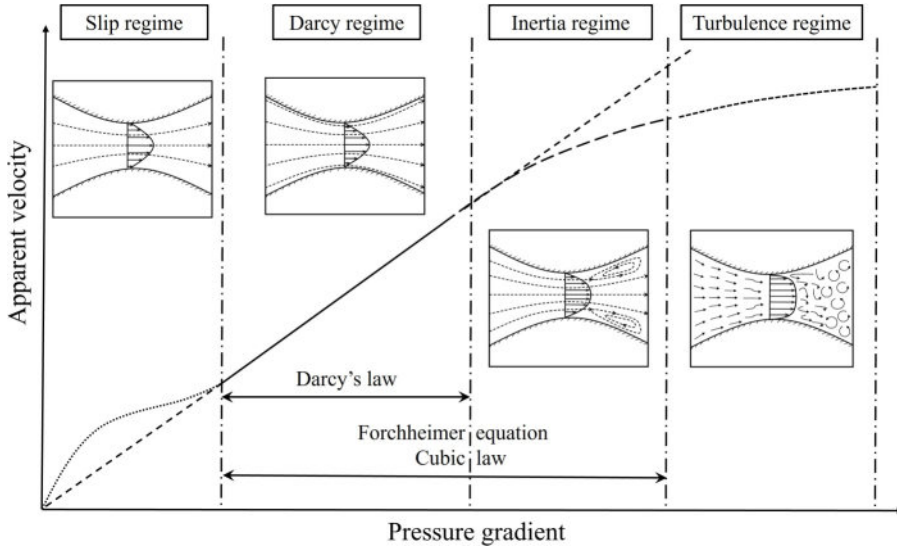


FIG. 2. The apparent velocity vs pressure gradient curves of four flow regimes. The horizontal axis represents the pressure gradient driving the flow, while the vertical axis represents the measured apparent velocity or flow rate. The curves in the graph depict trends and are not specific to particular samples or fluids, so no units are indicated.

where  $\rho$  ( $\text{kg m}^{-3}$ ) is the fluid density. If the square root of permeability is used as the characteristic length, an alternative form of the Forchheimer equation is

$$-\frac{\Delta P}{L} = \frac{\mu}{k}v + \frac{\rho\beta_2}{\sqrt{k}}v^2. \quad (3)$$

$\beta$  is the inertia coefficient. The difference between the two subscripts is that  $\beta_1$  ( $\text{m}^{-1}$ ) is dimensional and  $\beta_2$  is a dimensionless one. In addition, one form of the cubic law is

$$-\frac{\Delta P}{L} = \frac{\mu}{k}v + \frac{\gamma\rho^2}{\mu}v^3, \quad (4)$$

where  $\gamma$  is the dimensionless parameter of the nonlinear term. To further clarify the significance of the dimensionless criteria across different flow regimes, a scaling analysis of the constitutive equation is conducted. Under uniform one-dimensional conditions, Darcy's law can be expressed in differential form as follows:

$$-\frac{\partial P}{\partial x} = \frac{\mu}{k}u, \quad (5)$$

where  $u$  ( $\text{m s}^{-1}$ ) is the local mean velocity,  $P$  (Pa) is the pressure, and  $x$  (m) is the spatial coordinates, respectively. Dimensionless quantifications of the physical quantities are

$$\tilde{P} = \frac{P}{\rho v^2}, \quad \tilde{x} = \frac{x}{D}, \quad \tilde{u} = \frac{u}{v}, \quad (6)$$

where the characters with tildes are nondimensionalized, and  $D$  (m) is the characteristic size of the flow process. As a result, Eq. (5) is nondimensionalized as

$$-\frac{\rho v k}{\mu D} \frac{\partial \tilde{P}}{\partial \tilde{x}} = \tilde{u}. \quad (7)$$

A dimensionless number  $\frac{\rho vk}{\mu D}$  can thus be derived. Combining the Reynolds number  $\text{Re} = \frac{\rho v D}{\mu}$  yields the Darcy number  $\text{Da} = \frac{k}{D^2}$  (the ratio of the permeability to the characteristic length squared), which is small for most reasonably sized porous media [54]. Similarly, the two dimensionless forms of the Forchheimer equation are expressed as follows:

$$-\frac{\rho vk}{\mu D} \frac{\partial \tilde{P}}{\partial \tilde{x}} = \tilde{u} + \frac{\rho k \beta_1 v}{\mu} \tilde{u}^2, \quad (8)$$

$$-\frac{\rho vk}{\mu D} \frac{\partial \tilde{P}}{\partial \tilde{x}} = \tilde{u} + \frac{\rho \beta_2 \sqrt{k} v}{\mu} \tilde{u}^2. \quad (9)$$

The dimensionless number  $\frac{\rho k \beta_1 v}{\mu}$  of Eq. (8) is the Forchheimer number  $\text{Fo}$  defined by Zeng *et al.* [34], which physically represents the ratio of inertial forces to viscous forces, analogous to the Reynolds number. The other dimensionless quantity in Eq. (9) is denoted as  $\frac{\rho \beta_2 \sqrt{k} v}{\mu}$ . Due to the dimensionless nature of the inertia coefficient, we can redefine the  $\text{Rd}$  number as

$$\text{Rd} = \text{Re} \text{Da}^{1/2} = \frac{\rho v \sqrt{k}}{\mu}, \quad (10)$$

which mathematically shares the same form as the empirically used  $\text{Re}_k$  number by the previous researchers [55,56]. Yet, the  $\text{Rd}$  number has a dimensionless derivation process and a clear physical meaning. The  $\text{Re}$  number indicates the ratio of inertial forces to viscous forces and serves as a measure of the flow condition. Meanwhile, the  $\text{Da}$  number characterizes the magnitude of seepage capacity in the porous medium, which is commonly used to describe natural convection in porous media [57,58]. Consequently, the physical essence of the  $\text{Rd}$  number is the seepage ability and status of the fluid system within the porous medium. Derived from the inertial term of the Forchheimer equation and encompassing the Reynolds number, a higher  $\text{Rd}$  number signifies more pronounced inertial flow within the porous structure. Compared to the  $\text{Re}$  number, the  $\text{Rd}$  number offers a more comprehensive description of flow regime development within the porous medium, as it considers not only fluid properties but also the inherent characteristics of the porous structure. In contrast, the  $\text{Fo}$  number specifically characterizes the flow behavior of the fluid, without considering the intrinsic influence of the porous medium's structure. From a data processing perspective, the  $\text{Fo}$  number involves empirically derived inertial coefficients, introducing physical ambiguity. The  $\text{Rd}$  number relies solely on intrinsic parameters of both the fluid and porous medium, making it more convenient and aligned with the fundamental properties of dimensionless numbers. Therefore, the  $\text{Rd}$  number is more appropriate for describing of the development of the flow regimes within the porous medium.

### III. EXPERIMENTAL RESULTS

To validate the mechanistic explanation of flow regime delineation in the preceding sections, we have independently developed an experimental setup for gas seepage. The schematic diagram of this experimental setup is delineated in Fig. 3(a). The maximum upstream pressure, facilitated by the compressor, reaches 0.7 MPa. The TY-5 triaxial core holder can accommodate samples with a diameter of 25.4 mm and lengths ranging from 25 to 80 mm, while maintaining confining pressures between 0 and 50 MPa. A hydraulic pump is used to apply confining pressures. The downstream directly connects to the atmosphere, maintaining atmospheric pressure. For the measurement of low flow rates, a soap film flowmeter is utilized, while high flow rates are measured with a thermal gas flowmeter. Compressed air serves as the experimental medium. The porous medium samples are artificial cores formed through sintering and solidification. Quartz sand is used as the framework for the porous structure, with epoxy resin serving as the binder. These samples have a standardized size, with a diameter ( $D$ ) of 25 mm and a length ( $L$ ) of 50 mm. Ten samples with different values of permeability are utilized and displayed in Fig. 3(b). The porosity and pore size information for all samples are listed in Table I.

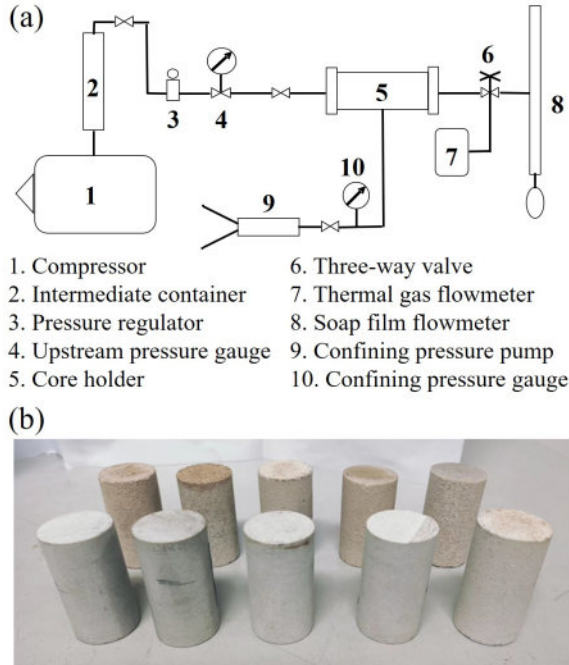


FIG. 3. Experimental setup for gas seepage: (a) Schematic diagram of the experimental device. The thermal gas flowmeter and the soap film flowmeter are used separately. (b) Physical diagram of artificial core samples with different permeability.

Throughout the entirety of the experimental procedure, precise control over the upstream pressure was achieved through regulating the pressure control valve. For samples with high permeability, the upper limit of the upstream pressure was determined by the compressor's capacity. Simultaneously, a constant confining pressure of 2 MPa was applied to prevent potential risks of sample deformation, fracturing, or failure. To ensure accurate flow rate measurements, the data from three separate measurements were averaged to obtain the corresponding flow rate under stable conditions. Given the consistency across multiple datasets, with an error margin of approximately 1%, it was decided not to include error bars in the presentation, and the manuscript only reports

TABLE I. Parameters of core samples.

Sample	Material	Porosity (%)	Pore size ( $\mu\text{m}$ )	Permeability (mD)
S1	Artificial rock core (quartz sand+epoxy resin)	5.35	1.46	0.32
S2		15.80	1.19	1.16
S3		12.98	1.86	5.00
S4		25.33	2.38	43.94
S5		28.74	4.81	89.91
S6		25.15	13.13	247.6
S7		26.36	11.95	306.0
S8		27.72	14.61	397.2
S9		28.92	25.66	543.4
S10		35.45	29.15	685.2

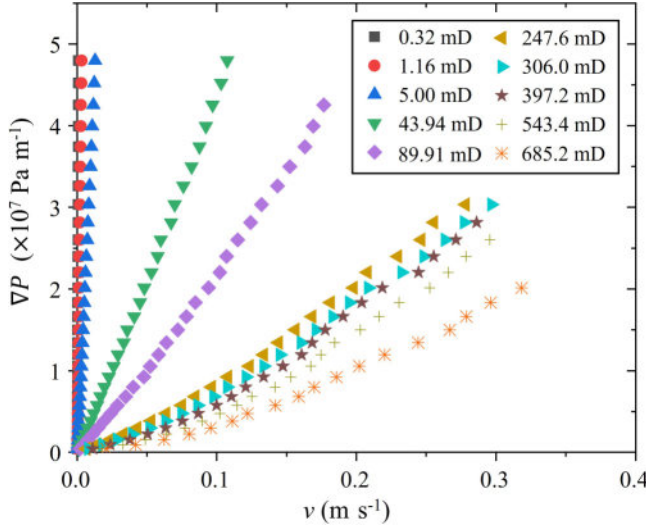


FIG. 4. Integral pressure gradient vs apparent velocity of ten samples. The data of several samples deviating from linearity indicate the presence of the inertia effect. The original data can be viewed from Ref. [59].

the mean values. An estimate of the temperature change inside the porous medium due to gas expansion was made, based on the maximum pressure difference used. In the case of a sevenfold gas expansion, internal heat conduction of the porous medium was approximated using a cylindrical heat conduction model with internal heat sources. The estimated temperature difference between the inside and outside is around 4 K, which is within the acceptable error range. The assumption that the overall temperature of the porous medium is consistent with the external temperature holds.

The obtained data need to exclude the compressibility effect of gas by preprocessing. Combining the gas equation of state and considering differential mass flow, the Forchheimer equation for compressible gas is expressed as follows:

$$-\frac{P_d^2 - P_u^2}{2P_d L} = \frac{\mu}{k} v + \beta \rho v^2, \quad (11)$$

where  $P_u$  (Pa) is upstream pressure, and  $P_d$  (Pa) is downstream pressure. Thus, the integral pressure gradient  $\nabla P$  ( $\text{Pa m}^{-1}$ ) can be defined as  $\nabla P = -\frac{P_d^2 - P_u^2}{2P_d L}$ . The pressure gradient in the following paragraphs refers to the integral pressure gradient. For the error analysis of the data, the uncertainty of flow rate  $Q$  is 2% based on gas flowmeter error. The uncertainty of upstream pressure  $P_u$  is 1% given by pressure gauge error. The error of length  $L$  and diameter  $d$  of the artificial core sample is 1% and 0.05%, respectively. According to the uncertainty equation, the error of the apparent velocity is about 2%, and the maximum error of the integral pressure gradient is less than 4%. It can be considered that all the experimental data in this work are within the acceptable range of error.

The  $\nabla P-v$  diagram is constructed using experimental data from 10 samples to provide a visual representation, as depicted in Fig. 4. Values of permeability are determined through linear regression fitting within the Darcy regime. It is evident from the plot that the data for several samples exhibit deviations from linearity, highlighting the presence of the inertia effect.

#### A. Flow regime division

Flow regime classification relies primarily on the graph calibration method, such as distinguishing various slopes of apparent velocity curves using hydraulic gradients. The relative pressure drop (RPD), defined as the ratio of the pressure gradient to velocity  $\text{RPD} = -\frac{\Delta P}{Lv}$ , was introduced as the

criterion for identifying distinct flow regimes [60]. In this study, four flow regimes are identified using the RPD-velocity (RPD-v) diagram and delineated by observing changes in the slope of each data segment: (i) The slip regime: this occurs before the Darcy flow regime, characterized by data points with RPD values lower than those found in the Darcy regime. (ii) The Darcy regime: in this regime, the experimental data follow Darcy's law, and the RPD is represented as a stable constant independent of velocity. As a result, the data points are clustered around a straight line with a zero slope, which indicates the Darcy flow. (iii) The inertia regime: with the emergence of inertial effects, the relationship between the pressure gradient and velocity generally follows the description of the Forchheimer equation, and the RPD shows an approximately linear increase with velocity. Therefore, the dataset exhibits a positive slope, signifying the inertia regime. (iv) The turbulence regime: in this regime, due to the further increase in flow resistance, the linear slope is lower than that observed in the inertia regime, indicating turbulent flow behavior.

The division results of the RPD-v diagram are shown in Fig. 5, where the slip regime is observed only in samples with permeability values below 5 mD. In the slip regime, the RPD is smaller compared to the Darcy regime, indicating a lower ratio of pressure gradient to apparent velocity. According to Darcy's law, the permeability in this regime is relatively higher, corroborating the results attributed to the slip effect. The presence of slip effects can be confirmed by the Knudsen number ( $Kn = \lambda/d$ ), which is the ratio of the molecular mean free path  $\lambda$  to pore size  $d$  [61]. Throughout this study, the values of pore pressure have been maintained at relatively low levels, ensuring constancy in the product of the molecular mean free path and the pressure of the specific gas under isothermal conditions. As shown in Fig. 6(a), the Knudsen numbers for the first three samples are greater than 0.01, which indicates slip effects, consistent with the slip flow regime [62]. This confirms that slip effects are the main cause of the slip flow regime in gas percolation, and that the Knudsen number is a reliable criterion for identifying it. Moreover, drawing on previous experimental findings [9,17,24,63,64], as shown in Fig. 6(b), the main characteristic of the pre-Darcy flow mechanism for liquids is an increase in flow resistance, which leads to a decrease in permeability. In contrast, the experimental results for gas flow show an increase in permeability, consistent with the mechanisms for evaluating the pre-Darcy flow regime from the perspective of gas seepage. It is worth noting that the onset of the slip regime displays some data points with higher-than-expected values. On the one hand, at very low flow velocities, even minor measurement errors can be magnified, resulting in an increase in the RPD value. On the other hand, small debris within the core may obstruct the initial pressure differential from driving the flow, leading to a reduction in flow velocity. This behavior is similar to that observed with the threshold pressure gradient.

For samples with permeability exceeding 43.94 mD, the slip effect is weakened, leading to the disappearance of the slip regime due to the increase in pore size. The emergence of the inertia regime aligns with the results depicted in Fig. 5. When the permeability exceeds 247.6 mD, the turbulence regime emerges while the Darcy mechanism significantly diminishes.

### B. The onset criterion of the inertia regime

As mentioned earlier, there are primarily four criteria, including apparent velocity, the Reynolds number  $Re = \frac{\rho D v}{\mu}$ , the Forchheimer number  $Fo = \frac{k \beta_1 \rho v}{\mu}$ , and the Rd number  $Rd = \frac{\rho v \sqrt{k}}{\mu}$ . The combination of the Forchheimer number with its corresponding friction coefficient  $f = \frac{\Delta P}{L \beta_1 \rho v^2} = 1 + \frac{1}{Fo}$  facilitates qualitative analysis, as illustrated in Fig. 7. All the data from different researchers overlap together and are well concentrated on a straight line when  $Fo$  is less than 0.1 [65–68]. It is worth noting that the data for the present work are derived from 10 samples with varying values of permeability, and they show a high level of overall consistency. The deviation from the approximate straight line serves as the initial criterion for the onset of the inertia regime, typically ranging from 0.1 to 1, with most falling closer to 0.1. This observation is consistent with previous experimental results on quartz sand-filled gas flow [22], although simulation outcomes indicate deviations within

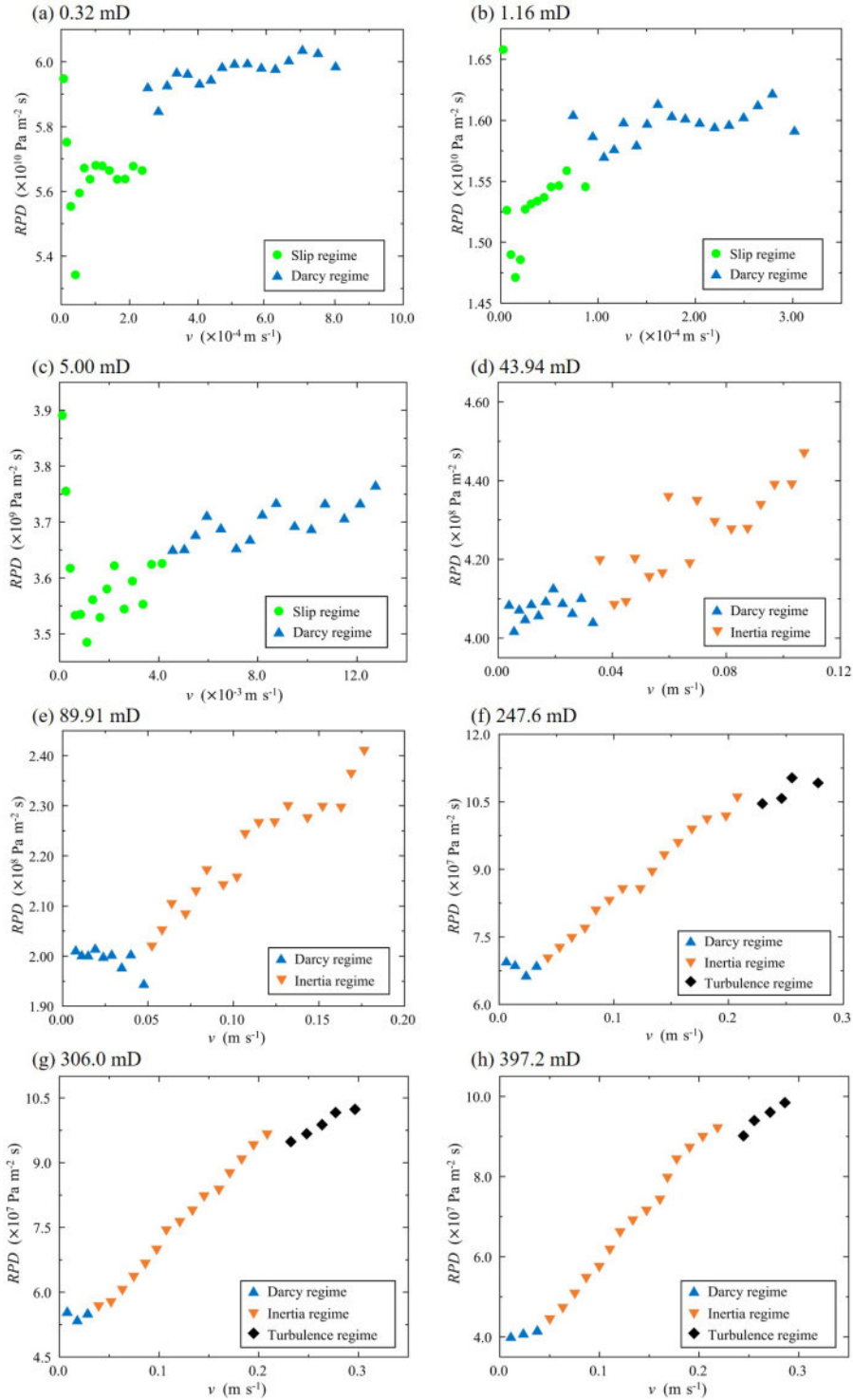


FIG. 5. Flow regime division of RPD- $v$  plot of eight samples with different permeability. Each sample distinguishes the main flow regimes as shown in the figure legend.

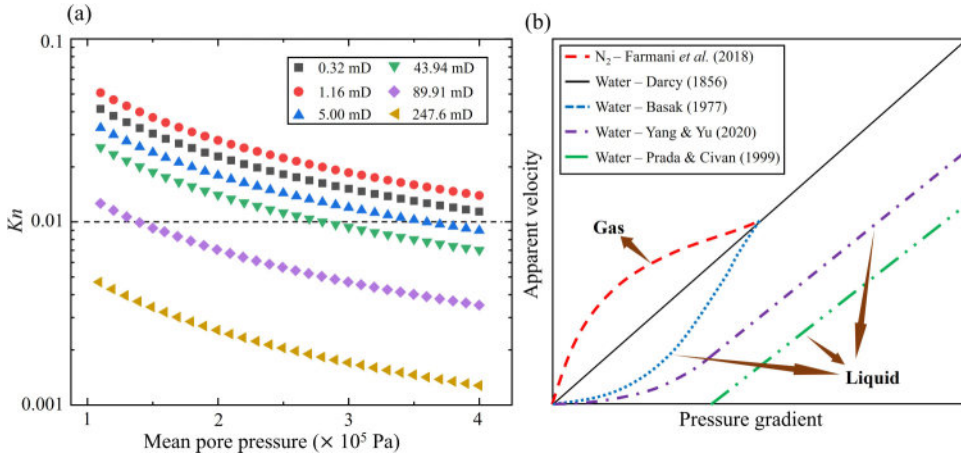


FIG. 6. Experimental validation of slip flow regimes: (a) Knudsen number vs pore pressure of six samples in the present work. (b) The previous experimental results on the pre-Darcy flow regime with different fluids. “Dashes” indicate nitrogen seepage results by Farmani *et al.* [63], “dots” represent water seepage results by Basak [17], “dash-dots” indicate water seepage results by Yang and Yu [24], and “dash-dot-dots” indicate water seepage results from Prada and Civan [64].

the range of 0.01–0.1 [69]. In general, a qualitative estimation criterion based on a  $Fo$  number of 0.1 has been widely accepted. The  $Fo$  number is advantageous because it allows for the aggregation and processing of a large amount of data, providing a clear visual indication of deviations within the inertia regime. However, it should be noted that this criterion does not offer a rigorous quantitative analysis.

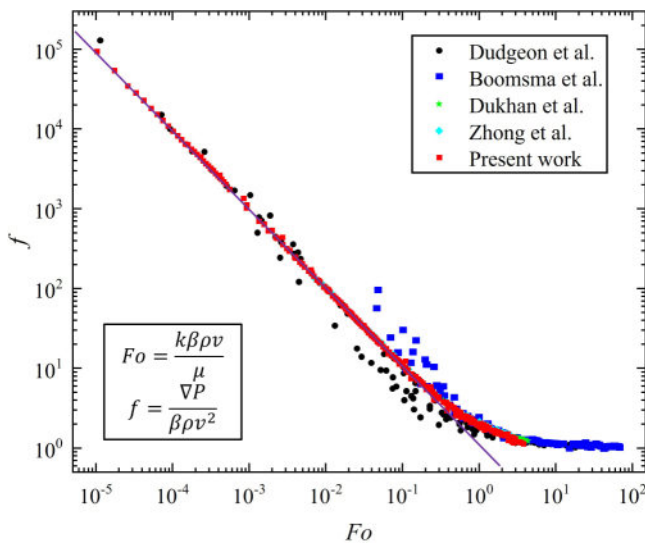


FIG. 7. The friction coefficient vs the Forchheimer number of the present work and previous work. The straight line only highlights data point concentration and deviation. The current work shows data from 10 samples with different values of permeability (0.32 – 685.2 mD). The data in previous works are sourced from the references, including Dudgeon *et al.* [66], Boomsma *et al.* [65], Dukhan *et al.* [67], and Zhong *et al.* [68].

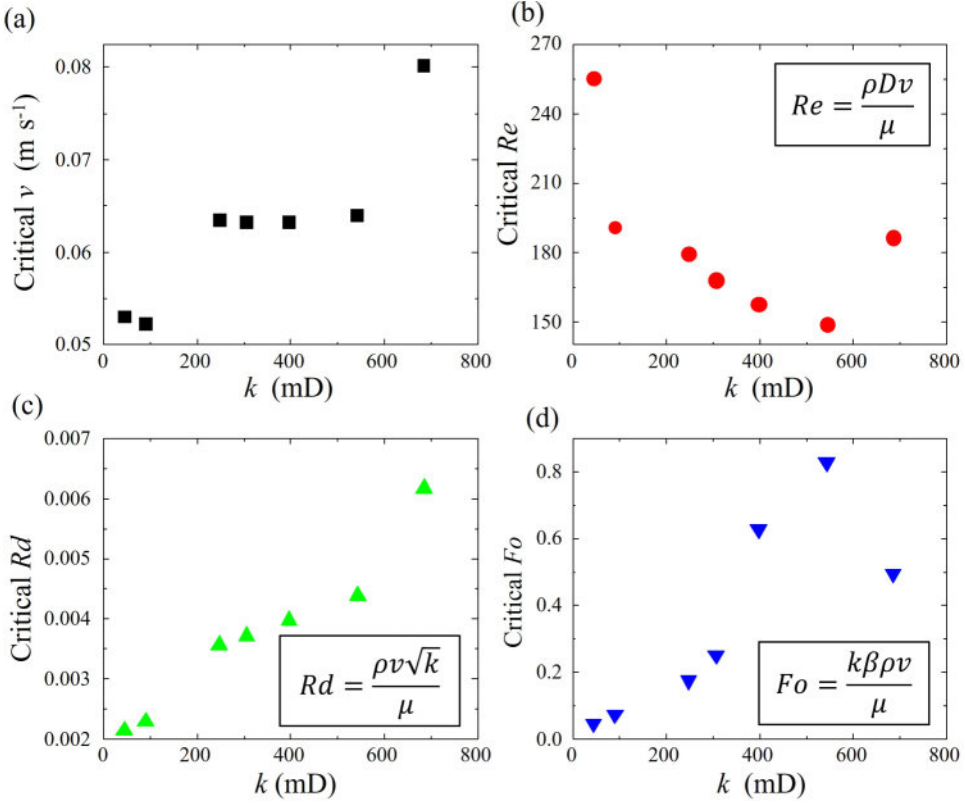


FIG. 8. The onset criterion of the inertia regime vs permeability by (a) apparent velocity  $v$ ; (b) Reynolds number  $Re$ ; (c)  $Rd$  number; and (d) Forchheimer number  $Fo$ . The criterion is that dimensionless permeability is less than 0.99.

Quantitative analysis of the onset criterion for the inertia regime requires introducing the dimensionless permeability  $k_s = \frac{\mu v}{k \nabla p}$ , which represents the ratio of viscous forces to the pressure gradient and quantifies the dissipation of viscous resistance relative to the pressure gradient. Ideally,  $k_s$  should approximate 1 in the absence of inertia effects. As the inertia resistance contributes to pressure gradient dissipation,  $k_s$  gradually decreases. Therefore, this parameter is critical for identifying the transition from the Darcy regime to the onset of the inertia regime. For practical engineering applications where high precision is not required, a threshold value of  $k_s < 0.95$  is often sufficient. In this study, we adopt a more conservative criterion of  $k_s < 0.99$  to define the onset of the inertia regime.

The variations in four critical criteria as a function of sample permeability are calculated and shown in Fig. 8. Although the critical apparent velocity shows an upward trend with permeability as shown in Fig. 8(a), the overall value is between 0.05 and 0.08 m s<sup>-1</sup>. The median value of 0.65 m s<sup>-1</sup> is used as the reference value of the critical apparent velocity with an error of below 15%. The critical Reynolds number initially exhibits a decreasing trend, with the final data point showing an increase as shown in Fig. 8(b). Overall, there is no apparent monotonic trend. It is not possible to directly explain this phenomenon solely based on the Reynolds number.

The critical  $Rd$  number tends to increase with the rise of permeability, as illustrated in Fig. 8(c). It follows a linear relationship in the following form:

$$Rd = \alpha k + \gamma, \quad (12)$$

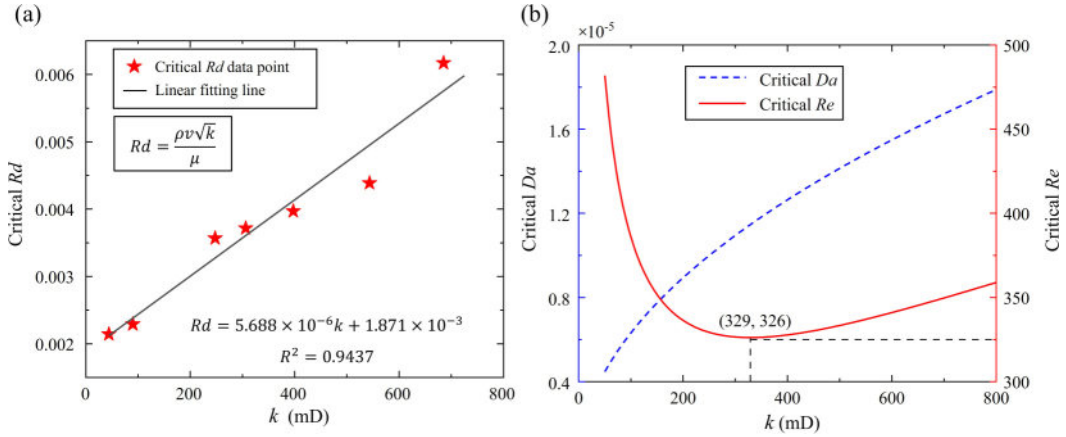


FIG. 9. The onset criterion of the inertia regime about the critical  $Rd$  number: (a) The critical  $Rd$  number vs permeability. The straight line is obtained by linear fitting of the data. (b) The  $Da$  number and  $Re$  number derived from the  $Rd$  number vs permeability. The critical  $Re$  number exhibits a minimum value.

where  $\alpha$  ( $\text{mD}^{-1}$ ) and  $\gamma$  are the fitting parameters. Based on the experimental data in this paper,  $\alpha = 5.688 \times 10^{-6}$ ,  $\gamma = 1.871 \times 10^{-3}$ . Figure 9(a) shows the linear fitting line and correlation. The correlation coefficient of this fitting is 0.9437, which indicates it can well reflect the relationship between critical  $Rd$  and permeability. The linear relationship reflects the dependence of the onset criterion for the inertial regime on permeability and is not a constant value. The  $Rd$  number for the onset criterion of the inertia regime can be calculated using Eq. (12) and can serve as a valuable reference for engineering applications. The definition of the  $Rd$  number allows for a more in-depth analysis of the relationship between the onset of the inertial regime and the generation of inertial effects. As permeability increases, the Darcy number ( $Da$ ) also rises, indicating an enhanced seepage capacity of the porous medium. However, permeability is not the only factor influencing the critical criteria. As shown in Fig. 9(b), the critical  $Re$  number, calculated based on the  $Rd$  number, follows a notable trend: it initially decreases and then increases, with a minimum value observed at a permeability of approximately 329 mD. For the values of permeability less than 329 mD, the critical Reynolds number increases as permeability decreases, suggesting that higher Reynolds numbers are required to initiate the transition into the inertia regime. This phenomenon correlates closely with our earlier computations of Knudsen numbers, highlighting the significant role of the slip effect. Specifically, for samples with permeability below 329 mD, slip effects are more pronounced, with this influence becoming more noticeable at lower permeabilities. Consequently, stronger inertial effects are needed at higher Reynolds numbers for the inertia regime to manifest in observable parameters such as apparent velocity and pressure gradient. For permeabilities greater than 329 mD, a slight but noticeable increase in the critical Reynolds number is observed. In other words, when slip flow effects are negligible, higher permeability also requires a higher critical Reynolds number to reach the inertia regime. This can be attributed to the general trend where increased permeability leads to larger pore diameters and reduced tortuosity. As a result, the formation of inertial recirculation or cores becomes more difficult, requiring a higher Reynolds number to generate sufficient inertial effects and transition into the inertial regime. In conclusion, the critical  $Rd$  number, as determined by Eq. (12), provides a reliable onset criterion for the inertia regime, offering valuable reference values for engineering applications. Moreover, the  $Rd$  number definition provides a mechanistic framework to explain both the onset of the inertial regime and the development of inertial effects.

The critical  $Fo$  number exhibits an upward trend with increasing permeability. However, it decreases in the case of the last sample, as shown in Fig. 8(d). This observed phenomenon can be

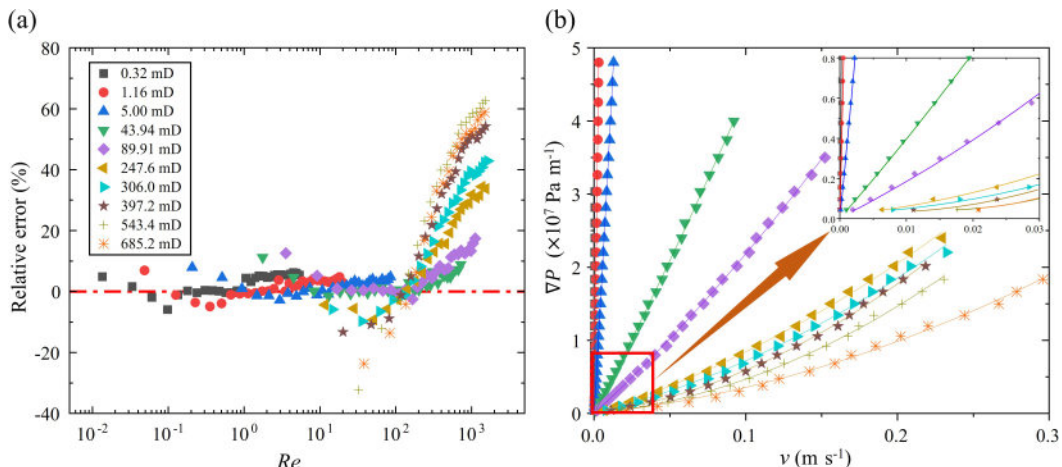


FIG. 10. Validation of the descriptive capability of equations: (a) The relative error vs Reynolds number  $Re$ . The relative error is calculated from the pressure gradient of the experimental data and the pressure gradient obtained by fitting Darcy's law. The straight line represents compliance with Darcy's law. (b) Fitting curves of the Forchheimer equation and experimental data points. The enlarged view of the low-velocity region highlights the Forchheimer equation's compatibility in describing the Darcy flow regime.

attributed to two primary factors. First, the behavior of critical  $Fo$  closely resembles that of critical  $Rd$ , both of which rise with increasing permeability. The deviation observed in the last sample is attributed to measurement fluctuations. Second, as permeability increases, the critical  $Fo$  follows a parabolic trajectory, initially reaching a peak before declining. A comprehensive understanding of this trend necessitates further measurements involving samples with higher values of permeability.

### C. Applicability of equations

From a theoretical perspective, the constitutive equation primarily incorporates Darcy's law, the Forchheimer equation, and the cubic law. Initial validation focuses on the applicability of Darcy's law by extending linear fitting results from the Darcy regime to all flow regimes. The relative error is quantitatively defined as  $\varepsilon = \frac{\Delta P - \Delta P_0}{\Delta P}$ , where  $\Delta P_0$  represents the pressure gradient obtained from the linear fitting. This metric is used to compare experimental data with the pressure gradients predicted by the fitting. Figure 10(a) presents the variation of relative error with Reynolds number. Initially, the relative error remains close to zero, indicating that deviations in the slip regime are relatively minor compared to those in the inertia regime. However, when Reynolds numbers exceed approximately 100, a significant increase in relative error occurs, demonstrating that the applicability of Darcy's law is largely limited to the Darcy regime. The effectiveness of the Forchheimer equation is validated by simultaneously fitting data from both the Darcy and inertia regimes. Figure 10(b) presents the fitting curves for 10 samples alongside the experimental data. A magnified view of the Darcy region reveals approximate linearity, confirming that the Forchheimer equation provides a compatible description of flow behavior within the Darcy regime.

The applicability of the Forchheimer equation and cubic law can be compared by fitting the Darcy and inertial regimes of the Darcy regime and the inertia regime of the last seven samples, respectively. The correlation coefficients by two fitting methods are presented in Fig. 11. The fitting correlation coefficient of the cubic law decreases significantly with the increase of sample permeability, indicating that the applicability is lower than the Forchheimer equation. However, at low permeability, the correlation coefficient of the cubic law is close to that of the Forchheimer equation. This result is consistent with the experimental results [70] and the numerical simulation

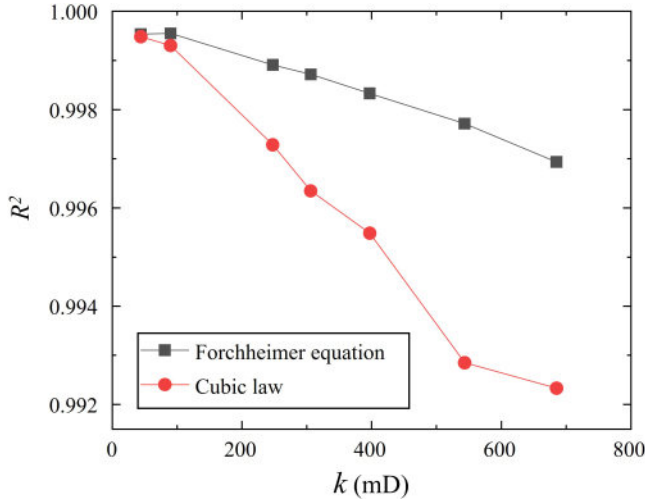


FIG. 11. The fitting correlation coefficients of the Forchheimer equation and cubic law vs permeability. Only seven samples existing in the inertia regime are used for comparison.

results [71] and supports the derivation of the cubic term with weak inertia from Mei *et al.* [21], that is, the cubic law is only effective at low velocity.

The Forchheimer equation demonstrates superior applicability, although it requires the inclusion of an unknown inertial coefficient [72]. There are two forms of the Forchheimer equation, each defining the inertia coefficient differently:  $\beta_1$ , which has dimensions of  $\text{m}^{-1}$ , and  $\beta_2$ , which is dimensionless. Notably, for the first five samples, Fig. 12(a) shows a noticeable upward trend in  $\beta_2$ . This allows for an effective fit of the inertia coefficient  $\beta_2$  as a function of permeability, represented by the following equation:

$$\beta_2 = Ak^n + B, \tag{13}$$

where  $A$ ,  $B$ , and  $n$  are the fitting parameters. The unit of  $k$  is mD, which is  $10^{-15} \text{ m}^2$ . According to the data fitting in the present work,  $A = 3.694 \times 10^{-11}$ ,  $B = 66.31$ ,  $n = 4.822$ . The empirical

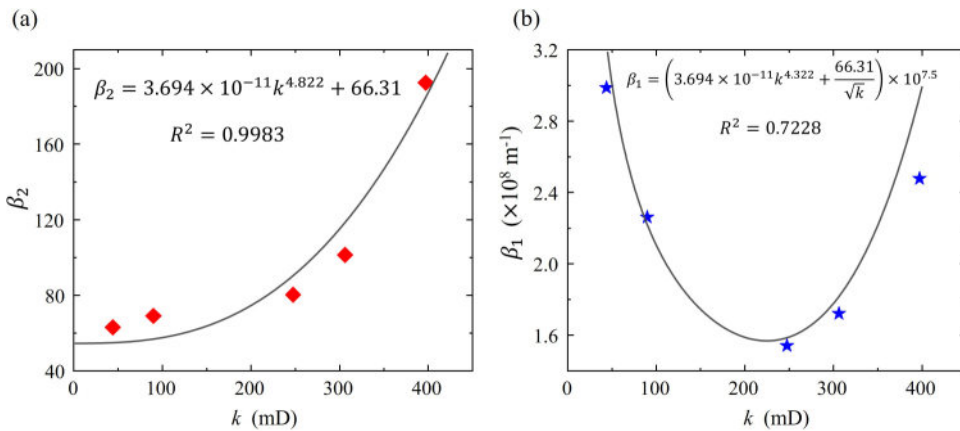


FIG. 12. The correlation curves and data points of inertia coefficient vs permeability: (a) dimensionless  $\beta_2$ ; (b) dimensional  $\beta_1$ .

correlation is shown in Fig. 12(a), with its dimensions hidden in the fitting parameters. The correlation coefficient  $R^2 = 0.9983$ , indicating a very high correlation. Therefore, the correlation in Eq. (13) can be used for the samples within a certain permeability range to provide a reliable reference for the inertia coefficient  $\beta_2$ .

Combining the relationship between two inertia coefficients  $\beta_1 = \frac{\beta_2}{\sqrt{k}}$ , the relation between inertia coefficient  $\beta_1$  and the permeability  $k$  can be deduced:

$$\beta_1 = \left( Ak^{n-0.5} + \frac{B}{\sqrt{k}} \right) \times 10^{7.5}, \quad (14)$$

where the unit of  $k$  is mD and the unit of  $\beta_1$  is  $\text{m}^{-1}$ . The constant coefficient at the end of the formula (14) is used to balance two dimensions. A comparison of the calculated results and experimental data is shown in Fig. 12(b) with a correlation coefficient  $R^2 = 0.7228$ . The results show that the error is relatively larger. The relationship (14) of  $\beta_1$  can provide a reference for scenes with lower precision requirements.

#### IV. CONCLUSIONS

This study presents a comprehensive categorization of gas flow regimes in porous media, integrating physical insights to identify four distinct regimes: the slip regime, the Darcy regime, the inertia regime, and the turbulence regime. Through scaling analysis of the Forchheimer equation, we redefine a dimensionless number,  $R_d$ , which provides a more physically grounded explanation for the transition to the inertia regime. The categorization of flow regimes has been validated through the independent construction of a gas seepage experimental platform.

The results confirm that the Kn number for the pre-Darcy regime is consistent with an explanation based on slip effects, thereby supporting the classification of the slip regime. For the inertia regime, the Forchheimer number proves effective for qualitative analysis. However, a more precise quantitative trend analysis requires further validation through high velocity seepage experiments. The critical  $R_d$  number shows a linear relationship with increasing permeability. This relationship suggests that a minimum critical Re number exists as permeability increases. Under low-permeability conditions, slip effects delay the transition into the inertia regime, while under high-permeability conditions, factors such as larger pore sizes or reduced tortuosity may hinder the development of inertial backflow.

Additionally, in characterizing both the Darcy and inertia flow regimes, the Forchheimer equation proves to have superior applicability compared to the cubic law. Its inertial coefficient can be determined through appropriate fitting correlations. In summary, this study provides valuable theoretical insights and experimental results for the classification of gas flow regimes and the use of dimensionless criteria within porous media. These findings offer substantial scholarly references for further research in related fields.

#### ACKNOWLEDGMENTS

This work is financially supported by the NSF of China (Grants No. U1837602 and No. 12272207) and the National Key Research and Development Program of China (Grant No. 2019YFA0708704).

M.W. conceived and promoted this work, M.Z. performed the experiment and analysis, M.Z. wrote the paper, and Z.T., Y.H., and M.W. revised the text.

## APPENDIX

The appendix presents the experimental conditions and critical criteria used by previous researchers for the critical onset of inertial effects in the form of a table. The experimental results indicate that using different criteria will produce different critical values, which also supports the necessity of this work (Table II).

TABLE II. A summary of the experimental study on the onset criterion of the inertia regime is presented in Table II. No entry indicates that the criterion for this study does not require a characteristic size.

Author	Material	Fluid	Criterion	Characteristic length	Critical value
Ergun [73]	Packed bed: Granular material	Gas	$Re_v = \frac{\rho dv}{\mu} \frac{1}{1-\phi}$	$d$ : filler diameter	3 – 10
Scheidegger [74]	Packed bed: Granular material	Water	$Re = \frac{\rho dv}{\mu}$	$d$ : filler diameter	0.1 – 75
Dybbs and Edwards [49]	Packed bed: glass bead/rod	Dye/water	$Re = \frac{\rho dv}{\mu}$	$d$ : filler diameter	1 – 10
Fand <i>et al.</i> [11]	Packed bed: glass bead	Water	$Re = \frac{\rho dv}{\mu}$	$d$ : filler diameter	2.3
Antohe <i>et al.</i> [60]	Compressed porous aluminum alloy	Poly- $\alpha$ -olefine /air	$Re_k = \frac{\rho \sqrt{k} v}{\mu}$	$\sqrt{k}$	1
Boomsma and Poulikakos [65]	Metal Foam	Water	$v$ ( m s <sup>-1</sup> ) $Re_k = \frac{\rho \sqrt{k} v}{\mu}$	$\sqrt{k}$	0.074 – 0.110 14.2 – 26.5
Yamada <i>et al.</i> [29]	Packed bed: gravel	Water	$Re = \frac{\rho dv}{\mu}$	$d$ : filler diameter	1
Moutsopoulos <i>et al.</i> [75]	Packed bed: gravel	Water	$Re = \frac{\rho dv}{\mu}$	$d$ : filler diameter	42
Zhong <i>et al.</i> [56]	Porous metal resistance	Air	$Re_k = \frac{\rho \sqrt{k} v}{\mu}$	$\sqrt{k}$	0.1
Dukhan <i>et al.</i> [67]	Metal Foam	Water	$v$ ( m s <sup>-1</sup> ) $Re_k = \frac{\rho \sqrt{k} v}{\mu}$	$\sqrt{k}$	0.02 1.9 – 6.4
Yang <i>et al.</i> [25]	Packed bed: granular material	Water	Apparent velocity		3.90 – 10.78
Li <i>et al.</i> [22]	Packed bed: quartz sand	Water	$Fo = \frac{\beta \rho k_F v}{\mu}$		0.1
Shi <i>et al.</i> [30]	Packed bed: limestone particles	Water	$Re_k = \frac{\rho \sqrt{k} v}{\mu}$	$\sqrt{k}$	0.02 – 0.03

[1] M. Mukherjee and V. Vishal, Gas transport in shale: A critical review of experimental studies on shale permeability at a mesoscopic scale, *Earth-Sci. Rev.* **244**, 104522 (2023).

[2] H. Ates, S. L. Eichmann, R. Vaidya, A. Gupta, and R. Mesdour, Risk assessment on the impact of non-darcy flow on unconventional well performance, *Gas Sci. Eng.* **124**, 205245 (2024).

- [3] H. E. Huppert and J. A. Neufeld, The fluid mechanics of carbon dioxide sequestration, *Annu. Rev. Fluid Mech.* **46**, 255 (2014).
- [4] C. E. Neuzil, Permeability of clays and shales, *Annu. Rev. Earth Planet. Sci.* **47**, 247 (2019).
- [5] W. C. Tan, L. H. Saw, H. S. Thiam, J. Xuan, Z. Cai, and M. C. Yew, Overview of porous media/metal foam application in fuel cells and solar power systems, *Renew. Sustain. Energy Rev.* **96**, 181 (2018).
- [6] J. Kang and M. Wang, Brinkman double-layer model for flow at a free-porous interface, *Int. J. Mech. Sci.* **263**, 108770 (2024).
- [7] Z. Tian, D. Zhang, G. Zhou, S. Zhang, and M. Wang, Compaction and sintering effects on scaling law of permeability-porosity relation of powder materials, *Int. J. Mech. Sci.* **256**, 108511 (2023).
- [8] M. Zhang, Y. Wang, Z. Tian, and M. Wang, A robust data processing method for pulse-decay measurement of tight materials, *Int. J. Mech. Sci.* **274**, 109270 (2024).
- [9] H. Darcy, *Les Fontaines Publiques de la Ville de Dijon* (Victor Dalmont, 1856).
- [10] A. Firoozabadi and D. L. Katz, An analysis of high-velocity gas flow through porous media, *J. Pet. Tech.* **31**, 211 (1979).
- [11] R. M. Fand, B. Kim, A. Lam, and R. T. Phan, Resistance to the flow of fluids through simple and complex porous media whose matrices are composed of randomly packed spheres, *J. Fluid Eng.* **109**, 268 (1987).
- [12] Z. Tian, D. Zhang, Y. Wang, G. Zhou, S. Zhang, and M. Wang, Inertial solution for high-pressure-difference pulse-decay measurement through microporous media, *J. Fluid Mech.* **971**, R1 (2023).
- [13] H. Hansika, M. S. A. Perera, and S. K. Matthai, Effects of inertia on fluid flow in fractured rock masses: A comprehensive review, *Gas Sci. Eng.* **123**, 205240 (2024).
- [14] J. A. Rushing, K. E. Newsham, P. M. Lasswell, J. C. Cox, and T. A. Blasingame, *Klinkenberg-Corrected Permeability Measurements in Tight Gas Sands: Steady-State Versus Unsteady-State Techniques*, SPE Annual Technical Conference and Exhibition, Houston, Texas (2004).
- [15] M. Wang, X. Lan, and Z. Li, Analyses of gas flows in micro- and nanochannels, *Int. J. Heat Mass Trans.* **51**, 3630 (2008).
- [16] H. Sun, J. Yao, D.-y. Fan, C.-c. Wang, and Z.-x. Sun, Gas transport mode criteria in ultra-tight porous media, *Int. J. Heat Mass Trans.* **83**, 192 (2015).
- [17] P. Basak, Non-darcy flow and its implications to seepage problems, *J. Irrig. Drain. Div.* **103**, 459 (1977).
- [18] N. Dukhan, Ö. Bağcı, and M. Özdemir, Experimental flow in various porous media and reconciliation of forchheimer and ergun relations, *Exp. Therm Fluid Sci.* **57**, 425 (2014).
- [19] P. Kundu, V. Kumar, and I. M. Mishra, Experimental and numerical investigation of fluid flow hydrodynamics in porous media: Characterization of pre-darcy, darcy and non-darcy flow regimes, *Powder Technol.* **303**, 278 (2016).
- [20] P. Forchheimer, Wasserbewegung durch boden, *Z. Ver. Deutsch. Ing.* **45**, 1782 (1901).
- [21] C. C. Mei and J.-L. Auriault, The effect of weak inertia on flow through a porous medium, *J. Fluid Mech.* **222**, 647 (1991).
- [22] Z. Li, J. Wan, K. Huang, W. Chang, and Y. He, Effects of particle diameter on flow characteristics in sand columns, *Int. J. Heat Mass Trans.* **104**, 533 (2017).
- [23] F. Siddiqui, M. Y. Soliman, W. House, and A. Ibragimov, Pre-darcy flow revisited under experimental investigation, *J. Anal. Sci. Technol.* **7**, 2 (2016).
- [24] S. Yang and Q. Yu, Experimental investigation on the movability of water in shale nanopores: A case study of carboniferous shale from the qaidam basin, china, *Water Resour. Res.* **56**, e2019WR026973 (2020).
- [25] X. Yang, T. Yang, Z. Xu, and B. Yang, Experimental investigation of flow domain division in beds packed with different sized particles, *Energies* **10**, 1401 (2017).
- [26] Ö. Bağcı and N. Dukhan, Experimental hydrodynamics of high-porosity metal foam: Effect of pore density, *Int. J. Heat Mass Trans.* **103**, 879 (2016).
- [27] X. Wang and J. J. Sheng, Pore network modeling of the non-darcy flows in shale and tight formations, *J. Pet. Sci. Eng.* **163**, 511 (2018).
- [28] Y. Yao, G. Li, and P. Qin, Seepage features of high-velocity non-darcy flow in highly productive reservoirs, *J. Nat. Gas Sci. Eng.* **27**, 1732 (2015).

- [29] H. Yamada, F. Nakamura, Y. Watanabe, M. Murakami, and T. Nogami, Measuring hydraulic permeability in a streambed using the packer test, *Hydrol. Proc.* **19**, 2507 (2005).
- [30] W. Shi, T. Yang, and S. Yu, Experimental investigation on non-darcy flow behavior of granular limestone with different porosity, *J. Hydrol. Eng.* **25**, 06020004 (2020).
- [31] M. Pauthenet, Y. Davit, M. Quintard, and A. Bottaro, Inertial sensitivity of porous microstructures, *Transp. Porous Media* **125**, 211 (2018).
- [32] H. Ma and D. W. Ruth, The microscopic analysis of high forchheimer number flow in porous media, *Transp. Porous Media* **13**, 139 (1993).
- [33] D. Ruth and H. Ma, On the derivation of the forchheimer equation by means of the averaging theorem, *Transp. Porous Media* **7**, 255 (1992).
- [34] Z. Zeng and R. Grigg, A criterion for non-darcy flow in porous media, *Transp. Porous Media* **63**, 57 (2006).
- [35] Z. Wang, M. Wang, and S. Chen, Coupling of high knudsen number and non-ideal gas effects in microporous media, *J. Fluid Mech.* **840**, 56 (2018).
- [36] W.-M. Zhang, G. Meng, and Z.-K. Peng, Gaseous slip flow in micro-bearings with random rough surface, *Int. J. Mech. Sci.* **68**, 105 (2013).
- [37] P. Diwu, T. Liu, Z. You, B. Jiang, and J. Zhou, Effect of low velocity non-darcy flow on pressure response in shale and tight oil reservoirs, *Fuel* **216**, 398 (2018).
- [38] A. Roustaei, T. Chevalier, L. Talon, and I. A. Frigaard, Non-darcy effects in fracture flows of a yield stress fluid, *J. Fluid Mech.* **805**, 222 (2016).
- [39] K. E. R. Boettcher, M.-D. Fischer, T. Neumann, and P. Ehrhard, Experimental investigation of the pre-darcy regime, *Exp. Fluids* **63**, 42 (2022).
- [40] S. Liu and J. H. Masliyah, Single fluid flow in porous media, *Chem. Eng. Commun.* **148-150**, 653 (1996).
- [41] J. D. Sherwood and G. H. Meeten, The filtration properties of compressible mud filtercakes, *J. Pet. Sci. Eng.* **18**, 73 (1997).
- [42] X. Wang and J. J. Sheng, Discussion of liquid threshold pressure gradient, *Petroleum* **3**, 232 (2017).
- [43] X.-J. Gu, R. W. Barber, B. John, and D. R. Emerson, Non-equilibrium effects on flow past a circular cylinder in the slip and early transition regime, *J. Fluid Mech.* **860**, 654 (2019).
- [44] E. K. Ahangar, M. B. Ayani, and J. A. Esfahani, Simulation of rarefied gas flow in a microchannel with backward facing step by two relaxation times using lattice boltzmann method—slip and transient flow regimes, *Int. J. Mech. Sci.* **157-158**, 802 (2019).
- [45] H. Darabi, A. Ettehad, F. Javadpour, and K. Sepehrnoori, Gas flow in ultra-tight shale strata, *J. Fluid Mech.* **710**, 641 (2012).
- [46] L. Germanou, M. T. Ho, Y. Zhang, and L. Wu, Intrinsic and apparent gas permeability of heterogeneous and anisotropic ultra-tight porous media, *J. Nat. Gas Sci. Eng.* **60**, 271 (2018).
- [47] S. Pasquier, M. Quintard, and Y. Davit, Modeling flow in porous media with rough surfaces: Effective slip boundary conditions and application to structured packings, *Chem. Eng. Sci.* **165**, 131 (2017).
- [48] Z. Khalifa, L. Pocher, and N. Tilton, Regimes of flow through cylinder arrays subject to steady pressure gradients, *Int. J. Heat Mass Trans.* **159**, 120072 (2020).
- [49] A. Dybbs and R. V. Edwards, A new look at porous media fluid mechanics—darcy to turbulent, in *Fundamentals of Transport Phenomena in Porous Media*, edited by J. Bear and M. Y. Corapcioglu (Springer Netherlands, Dordrecht, 1984), pp. 199–256.
- [50] K. Vafai and C. L. Tien, Boundary and inertia effects on flow and heat transfer in porous media, *Int. J. Heat Mass Trans.* **24**, 195 (1981).
- [51] Ö. Bağcı, N. Dukhan, and M. Özdemir, Flow regimes in packed beds of spheres from pre-darcy to turbulent, *Transp. Porous Media* **104**, 501 (2014).
- [52] I. González-Neria, J. A. Yáñez-Varela, S. A. Martínez-Delgado, G. Rivadeneyra-Romero, and A. Alonzo-García, Analysis of the turbulent flow patterns generated in isotropic porous media composed of aligned or centered cylinders, *Int. J. Mech. Sci.* **199**, 106396 (2021).
- [53] B. D. Wood, X. He, and S. V. Apte, Modeling turbulent flows in porous media, *Annu. Rev. Fluid Mech.* **52**, 171 (2020).

- [54] W. Lyu and X. Wang, Stokes–darcy system, small-darcy-number behaviour and related interfacial conditions, *J. Fluid Mech.* **922**, A4 (2021).
- [55] K. Suga, Y. Okazaki, and Y. Kuwata, Characteristics of turbulent square duct flows over porous media, *J. Fluid Mech.* **884**, A7 (2020).
- [56] W. Zhong, X. Li, F. Liu, G. Tao, B. Lu, and T. Kagawa, Measurement and correlation of pressure drop characteristics for air flow through sintered metal porous media, *Transp. Porous Media* **101**, 53 (2014).
- [57] T. R. Vijayababu and S. Dhinakaran, Mhd natural convection around a permeable triangular cylinder inside a square enclosure filled with  $\text{Al}_2\text{O}_3\text{-H}_2\text{O}$  nanofluid: An lbm study, *Int. J. Mech. Sci.* **153-154**, 500 (2019).
- [58] T. R. Vijayababu and K. B. N.B., Significance of porous elliptical cylinder on the mhd natural convection, *Int. J. Mech. Sci.* **237**, 107792 (2023).
- [59] M. Zhang, Original data for “Gas flow regimes and transition criteria in porous media,” Mendeley Data, V1, 2025, doi: [10.17632/ydpf5yf4zb.1](https://doi.org/10.17632/ydpf5yf4zb.1).
- [60] B. V. Antohe, J. L. Lage, D. C. Price, and R. M. Weber, Experimental determination of permeability and inertia coefficients of mechanically compressed aluminum porous matrices, *J. Fluid Eng.* **119**, 404 (1997).
- [61] S. Ghadirzadeh and M. Kalteh, Lattice boltzmann simulation of temperature jump effect on the nanofluid heat transfer in an annulus microchannel, *Int. J. Mech. Sci.* **133**, 524 (2017).
- [62] C. Li, P. Xu, S. Qiu, and Y. Zhou, The gas effective permeability of porous media with klinkenberg effect, *J. Nat. Gas Sci. Eng.* **34**, 534 (2016).
- [63] Z. Farmani, R. Azin, R. Fatehi, and M. Escrochi, Analysis of pre-darcy flow for different liquids and gases, *J. Pet. Sci. Eng.* **168**, 17 (2018).
- [64] A. Prada and F. Civan, Modification of darcy’s law for the threshold pressure gradient, *J. Pet. Sci. Eng.* **22**, 237 (1999).
- [65] K. Boomsma and D. Poulikakos, The effects of compression and pore size variations on the liquid flow characteristics in metal foams, *J. Fluid Eng.* **124**, 263 (2002).
- [66] C. R. Dudgeon, An experimental study of the flow of water through coarse granular media, *La Houille Blanche* **52**, 785 (1966).
- [67] N. Dukhan, Ö. Bağcı, and M. Özdemir, Metal foam hydrodynamics: Flow regimes from pre-darcy to turbulent, *Int. J. Heat Mass Trans.* **77**, 114 (2014).
- [68] W. Zhong, X. Ji, C. Li, J. Fang, and F. Liu, Determination of permeability and inertial coefficients of sintered metal porous media using an isothermal chamber, *Appl. Sci.* **8**, 1670 (2018).
- [69] J. S. Andrade, U. M. S. Costa, M. P. Almeida, H. A. Makse, and H. E. Stanley, Inertial effects on fluid flow through disordered porous media, *Phys. Rev. Lett.* **82**, 5249 (1999).
- [70] M. Firdaouss, J.-L. Guermond, and P. Le Quéré, Nonlinear corrections to darcy’s law at low reynolds numbers, *J. Fluid Mech.* **343**, 331 (1997).
- [71] M. S. Newman and X. Yin, Lattice Boltzmann simulation of non-darcy flow in stochastically generated 2D porous media geometries, *SPE J.* **18**, 12 (2013).
- [72] A. Erić, D. Dakić, S. Nemoda, M. Komatina, and B. Repić, Experimental method for determining forchheimer equation coefficients related to flow of air through the bales of soy straw, *Int. J. Heat Mass Trans.* **54**, 4300 (2011).
- [73] S. Ergun, Fluid flow through packed columns, *J. Mater. Sci. Chem. Eng.* **48**, 89 (1952).
- [74] A. E. Scheidegger, *The Physics of Flow Through Porous Media*, 3rd ed. (University of Toronto Press, Toronto, 1974).
- [75] K. N. Moutsopoulos, I. N. E. Papaspyros, and V. A. Tsihrintzis, Experimental investigation of inertial flow processes in porous media, *J. Hydrol.* **374**, 242 (2009).